Nanocavity-Modulated Gate-Engineered InGaN Dopingless TFET: A Case Study for Breast Cancer Biosensing

Amir Khodabakhsh[1] – Reza Faraji[1] – Farnaz Jahandari[1] – Amir Amini[1,]*
[1] *Department of Electrical Engineering, WT.C., Islamic Azad University, Tehran, 1461944563, Iran*
[*] *Amir.Amini@iau.ac.ir*

ABSTRACT

This work presents a nanocavity-modulated gate-engineered InGaN dopingless tunnel field-effect transistor (TFET) as a case study for breast cancer biosensing. The proposed device combines charge-plasma source/drain formation with a retained tunneling gate and a dielectric-sensitive nanocavity positioned beneath the control-gate region. The cavity is intended to accommodate an immobilized recognition layer, captured breast-cancer-associated biomarkers, and the surrounding local fluid, while different biological conditions are represented through effective dielectric signatures rather than intact cells. Device behavior is investigated using two-dimensional TCAD simulations with a nonlocal band-to-band tunneling model and relevant carrier transport and recombination mechanisms. The sensing principle relies on dielectric modulation of the local electrostatic coupling, which alters the energy-band profile, tunneling barrier, carrier concentration, and drain-current response. The simulated results show clear separation between the air-filled reference state, the non-tumorigenic reference condition, and malignant-associated dielectric conditions. Key electrical indicators, including ON/OFF current ratio, average subthreshold swing, maximum transconductance, and ON-state current, exhibit strong and systematic variation with cavity permittivity. The proposed architecture therefore offers a promising route toward label-free, low-power, and electrically distinguishable biosensing using an InGaN tunneling platform.

Keywords: *InGaN TFET; Dopingless transistor; Nanocavity biosensor; Dielectric modulation; Breast cancer biosensing*

1. *INTRODUCTION*

Breast cancer remains one of the most prevalent malignancies among women and a major cause of cancer-related mortality worldwide [1], [2]. Although mammography, magnetic resonance imaging, and ultrasonography are widely used for clinical screening, their cost, accessibility, and performance limitations motivate the development of compact and sensitive complementary diagnostic platforms [3] to [6]. In this context, field-effect-transistor-based biosensors have received considerable attention because biochemical interactions can be directly converted into electrical signals while enabling label-free detection, miniaturization, rapid response, and low-power operation [1], [4], [7].

Among these approaches, dielectric-modulated FETs (DM-FETs) employ a functionalized sensing region in which captured biomolecular targets alter the effective dielectric environment and consequently modulate the gate-to-channel electrostatic coupling [8]. Experimental dielectric spectroscopy has reported clear differences between non-tumorigenic and malignant breast cell lines, and the corresponding effective dielectric conditions have subsequently been adopted in comparative DM-FET/TFET simulations [9] to [13]. These values should be interpreted as representative cell-line-associated effective dielectric signatures, rather than as the literal permittivities of intact cells, isolated biomarkers, or clinical fluids. Their strong dielectric contrast nevertheless provides a useful framework for evaluating electrical discrimination between healthy-reference and malignant-associated conditions.

Conventional MOSFET-based sensors become increasingly affected by short-channel effects and the thermally limited subthreshold swing as device dimensions are reduced [14], [15]. Tunnel FETs (TFETs), in contrast, rely on band-to-band tunneling (BTBT), offering the potential for steep switching and extremely low

OFF-state current, which are particularly attractive for low-power sensing applications [1], [16]. However, conventional TFETs generally require highly doped and abrupt source/drain junctions. Charge-plasma or dopingless architectures alleviate this requirement by using appropriate metal work functions to electrostatically induce carrier-rich regions, thereby reducing implantation-related complexity and random dopant fluctuations [1]. Gate-engineered InGaN dopingless TFETs have additionally demonstrated that a dedicated tunneling gate can locally enhance band bending and shorten the tunneling path near the source/channel junction [17].

In this work, a nanocavity-modulated gate-engineered InGaN dopingless TFET is investigated as a case study for breast cancer biosensing. The proposed structure retains the tunneling-gate-assisted charge-plasma architecture while introducing a functionalized dielectric-sensitive nanocavity beneath the control gate. Changes in the effective cavity permittivity modify the local electrostatics, BTBT process, and resulting drain current. Two-dimensional SILVACO ATLAS simulations are used to evaluate the sensing response through the energy-band profile, carrier distribution, I_{ON}/I_{OFF}, average subthreshold swing, transconductance, ON-state current, and dielectric sensitivity. The proposed approach aims to combine strong electrical discrimination with low-current and low-power operation in a compact label-free sensing platform.

2. *DEVICE STRUCTURE AND SIMULATION FRAMEWORK*

2.1 Device Structure and Biosensing Cavity

The device simulated in this study is a nanocavity-integrated $In_{0.75}Ga_{0.25}N$ gate-engineered dopingless TFET (Bio-TFET), obtained by modifying the baseline TFET architecture reported in [18], [19], as illustrated in Fig. 1. Two structural features of the reference design are carried over without change: the 10-nm InGaN body, and the 50-nm control gate. A 50 × 12 nm^2 nanocavity is etched exclusively beneath the control-gate region, and a 2-nm $HfO_2/SiO2$ layer is placed between this cavity and the InGaN body to electrically decouple the sensing region from the channel. The tunneling gate (TG) is deliberately retained at the source/channel junction: its electrostatic action builds a carrier-rich virtual pocket, raises the local electric field, and shortens the effective tunneling path. The complete set of structural parameters is summarized in Table 1.

Table 1. Main structural parameters [18,19]

Parameter	Value
InGaN body thickness	10 nm
Control-gate length	50 nm
Source length	100 nm
Drain length	100 nm
Tunneling-gate length	2 nm
Nanocavity length	50 nm
Nanocavity thickness	12 nm
Interfacial oxide thickness	2 nm
Control-gate work function	4.5 eV
TG work function	3.9 eV
Source-inducing metal	Pt, 5.93 eV
Drain-inducing metal	Hf, 3.9 eV

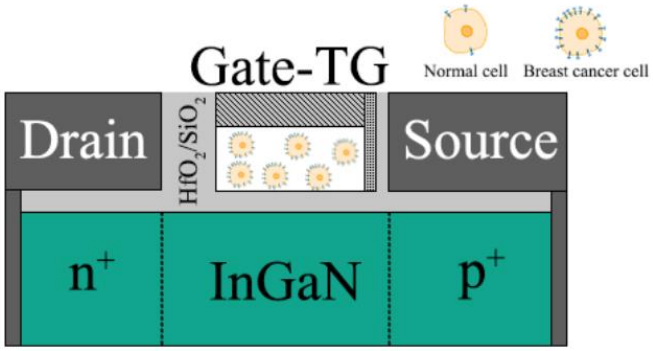


Fig. 1. Schematic cross-section of the proposed $In_{0.75}Ga_{0.25}N$ GEDL-TFET biosensor with the embedded nanocavity.

2.2. Charge-Plasma Operation and Material Parameters

Rather than relying on conventional chemical heavy-doping steps, the source and drain regions of the device are electrostatically induced through the charge-plasma (CP) technique [18], [20]. A high-work-function Pt contact establishes a hole-rich p^+ source region, while a lower-work-function Hf contact establishes an electron-rich n^+ drain region. Reliable CP formation requires the contact work functions and the semiconductor body thickness to jointly satisfy [20]

$$\Phi_{drain} < \chi_{semi} + Eg/2, \qquad \Phi_{source} > \chi_{semi} + Eg/2, \tag{1}$$

together with

$$t_{semi} < L_D = \sqrt{\varepsilon_{semi} \cdot V_T / qN} \tag{2}$$

in which χ_{semi}, E_g, ε_{semi}, N, and V_T correspond to the electron affinity, bandgap, permittivity, carrier concentration, and thermal voltage of the semiconductor, respectively [18], [20]. It should be emphasized that L_D here denotes the semiconductor Debye length governing charge-plasma formation.

All $In_{0.75}Ga_{0.25}N$ material parameters are adopted from the references [18], [21] to [23], are listed in Table 2. The comparatively low carrier effective masses characteristic of In-rich InGaN favor efficient band-to-band tunneling [20]. This composition is not an arbitrary theoretical choice: plasma-assisted molecular-beam epitaxy (PAMBE) has already produced chemically homogeneous In-rich InGaN films, and low-temperature MBE has achieved single-phase InGaN across virtually the entire alloy-composition range, evidence supporting the practical feasibility of the x = 0.75 composition adopted here [24], [25].

Table 2. $In_{0.75}Ga_{0.25}N$ material parameters [18], [21] to [23]

Parameter	Value
Bandgap, E_g	1.1125 eV
Electron effective mass	0.1025 m0
Light-hole effective mass	0.295 m0
Relative permittivity	12.75
Electron mobility	1050 cm²/V·s
Hole mobility	20 cm²/V·s

2.3. Nanocavity and Biological Representation

The 50 × 12 nm² nanocavity is not intended to house an entire breast cell; instead, it is sized to hold an immobilized recognition layer together with captured breast-cancer-associated biomarkers and the surrounding local fluid. A 2-nm oxide layer provides electrical isolation between this sensing cavity and the InGaN body. This choice is supported by prior work showing that ALD-grown HfO_2/SiO_2 forms a gate dielectric with favorable interfacial quality on III-nitride GaN/AlGaN surfaces, which supports the use of an ultrathin oxide sensing interface in the present structure [26], [27].

Selective biofunctionalization is achieved by patterning a thin Cr/Au coating on the cavity sidewalls and on non-gating sensing surfaces. The chromium layer promotes gold adhesion, while the gold layer offers a biocompatible surface onto which antibodies, aptamers, or other recognition elements can be immobilized via Au-thiol self-assembled monolayers [28], [29]. Restricting the metal coating to these regions avoids forming a continuous metallic screen between the control gate and the active InGaN sensing surface.

Rather than modeling entire cells inside the cavity, the biological environment is represented through effective cavity permittivities (κ_{eff}), summarized in Table 3 [30], [21].

Table 3. Effective cavity permittivities for representative conditions [3], [31]

Condition	κ_{eff}
Air	1
MCF-10A	4.5
HS578T	22
MDA-MB-231	24.5
MCF-7	27.5
T47D	32

MCF-10A serves as the non-tumorigenic control, while HS578T, MDA-MB-231, MCF-7, and T47D represent dielectric conditions associated with malignant cell lines. These permittivity values should be understood as comparative effective dielectric signatures rather than literal permittivities of intact cells or clinical fluids.

Figure 2 summarizes the proposed dielectric-modulation (DM) sensing concept from sample collection to electrical readout. Breast-cancer-associated biomarkers present in representative biofluids, such as blood, urine, or nipple aspirate fluid, are selectively captured by the functionalized receptor layer inside the sensing region. Biomarker binding modifies the local effective permittivity and the equivalent interfacial capacitance formed by the biomolecular layer, receptor layer, and semiconductor channel. This dielectric perturbation alters the gate-to-channel electrostatic coupling and consequently modulates the tunneling current of the InGaN TFET. The resulting electrical response is then processed by the external readout system, enabling discrimination between the reference and malignant-associated dielectric conditions without requiring intact cells to enter the nanocavity.

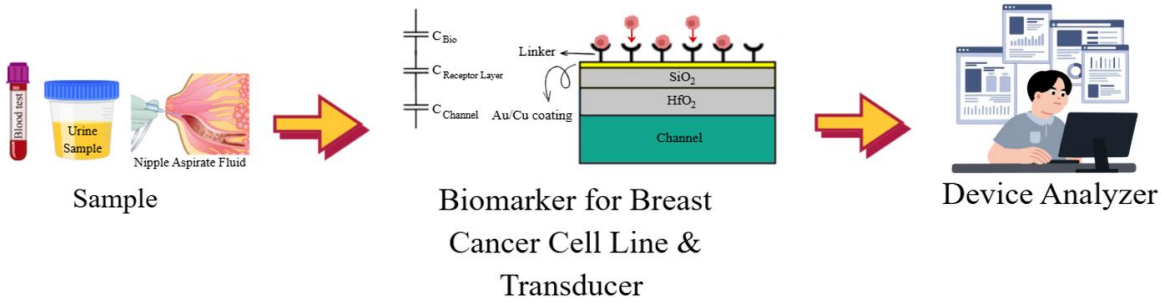


Fig. 2. Schematic illustration of the proposed DM biosensing workflow, including biofluid sampling, selective biomarker capture at the functionalized HfO_2/SiO_2 sensing interface, dielectric modulation of the channel electrostatics, and electrical readout.

2.4. TCAD Models

Device-level simulations are carried out in two dimensions using Silvaco ATLAS, which self-consistently solves Poisson's equation together with the electron and hole continuity equations. Because tunneling probability depends on how the energy bands vary spatially along the tunneling path, the nonlocal BTBT model is adopted throughout; this is also the formulation Silvaco specifically recommends for TFET simulation [32].

The simulation deck further incorporates Shockley-Read-Hall and Auger recombination, trap-assisted tunneling, Fermi-Dirac carrier statistics, and mobility models that depend on both carrier concentration and electric field. The numerical mesh is locally refined near the source/channel junction, the tunneling gate, the oxide/InGaN interface, and the nanocavity region, keeping the overall modeling approach consistent with previous TFET simulation framework [18], [20].

2.5. Fabrication Feasibility

A realistic process flow for the proposed device would combine PAMBE growth of the In-rich InGaN body with dielectric deposition, lithographic gate patterning, and selective cavity formation. This route is supported by prior experimental demonstrations of In-rich InGaN grown directly on Si and of single-phase InGaN obtained by low-temperature MBE across the full compositional range [24], [25]. The 2-nm $HfO_2/SiO2$ interfacial layer is compatible with thickness-controlled ALD-based dielectric deposition, and the 50-nm sensing window can be opened by selectively etching the upper dielectric/gate stack. A subsequent Au-based functionalization step would then yield a receptor-compatible sensing surface [26] to [29].

3. *RESULTS AND DISCUSSION*

3.1 Electrical analysis

To clarify the sensing mechanism, three representative cavity conditions are considered: the air-filled cavity (ready-to-use state), the healthy-cell-line-associated dielectric condition (κ_{eff} = 4.5, MCF-10A), and the diseased-cell-line-associated dielectric condition (κ_{eff} = 32, T47D). Figure 3(a) shows that the dielectric condition inside the cavity strongly modulates the energy-band profile near the source-channel junction. In the air-filled state, the electrostatic coupling is weakest, so the band bending is limited and the tunneling barrier remains relatively wide. As a result, the BTBT probability is strongly suppressed and the device remains in a very low-current standby condition. In addition, the post-junction barrier toward the channel/drain side remains relatively high, so thermionic carrier transport is also less favorable.

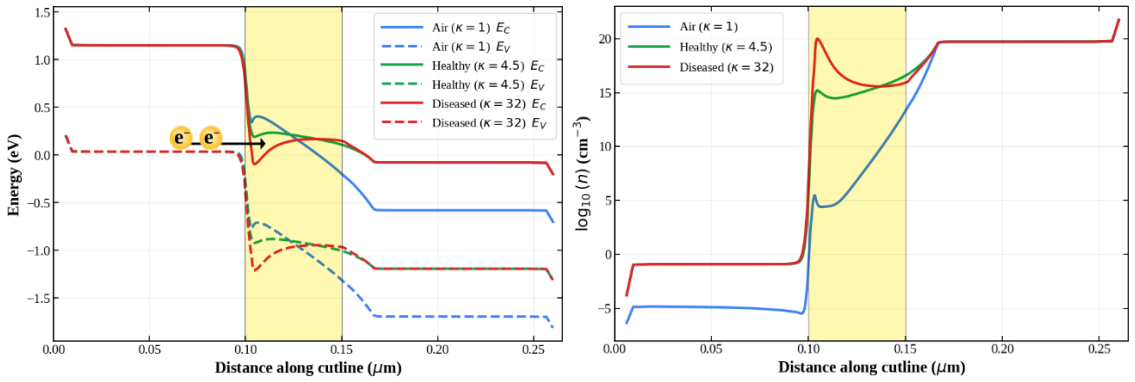


Fig. 3(a) Simulated conduction- and valence-band profiles, and **(b)** electron-concentration of the proposed biosensor TFET for air, healthy, and diseased cavity conditions.

When the cavity is filled with the healthy-condition dielectric, the local gate coupling becomes stronger and the source-channel bands bend more noticeably. This reduces the tunneling width and increases the BTBT rate compared with the air case. Consequently, the electron concentration near the junction increases, as shown in Fig. 3(b), and the device exhibits a clear rise in conduction. For the diseased high-κ_{eff} condition, the band modulation is the strongest, producing the narrowest effective tunneling barrier and the highest carrier accumulation near the tunneling junction. Therefore, the ON-state current enhancement is mainly governed by stronger BTBT injection, while the reduced barrier after tunneling also facilitates thermionic/drift transport toward the drain. These results confirm that the proposed device can clearly discriminate among standby, healthy, and diseased conditions through dielectric-modulated electrostatics at the heterojunction.

3.2 Electrical Performance and Low-Power Operation

At V_{GS}=1V and V_{DS}=0.5 V, the proposed sensor exhibits a pronounced electrical transition from the air-filled state to the biological conditions. The I_{ON}/I_{OFF} ratio increases from only 98 for air to 2.12×10^{5} for the healthy-reference condition (κ=4.5), and further reaches 9.11×10^{10}-1.73×10^{11} for the malignant-associated dielectric range (κ=22-32). Simultaneously, the average subthreshold swing decreases from 142 to 69 mV/dec and finally to 38.4–27.4 mV/dec. The average subthreshold swing is evaluated as [20]

$$SS_{avg} = \frac{V_{th}-V_{oFF}}{log_{(I_{v_{th}})}-\log(I_{v_{oFF}})} \tag{3}$$

while the transconductance is defined as [33]

$$g_m = \frac{dI_D}{dV_{GS}}, \qquad g_{m,max} = \max(g_m) \tag{4}$$

The maximum transconductance increases from 5.5 μS in air to 24 μS for the healthy condition and 41-53 μS for the malignant conditions. Likewise, I_{ON} increases from an almost negligible 2.6×10^{-15} A in the ready-to-use state to 0.831 μA for the healthy condition and 1.48-1.90 μA for the malignant range. Consequently, at V_{DS}=0.5 V, the corresponding ON-state power remains only about 0.74-0.95 μW in the malignant range, demonstrating strong electrical discrimination while preserving low-power operation.

As shown in Fig. 4, the proposed sensor exhibits a clear and monotonic electrical response as the effective cavity permittivity increases from the reference condition toward the malignant-associated range. The increase in I_{ON}/I_{OFF}, $g_{m,max}$, and I_{ON}, together with the reduction in SS_{avg}, confirms enhanced gate control and stronger tunneling modulation under higher-κ\kappa sensing conditions. The distinct separation between the healthy-reference region and the malignant-associated range demonstrates the suitability of these electrical metrics for reliable dielectric-based discrimination while maintaining low-current operation.

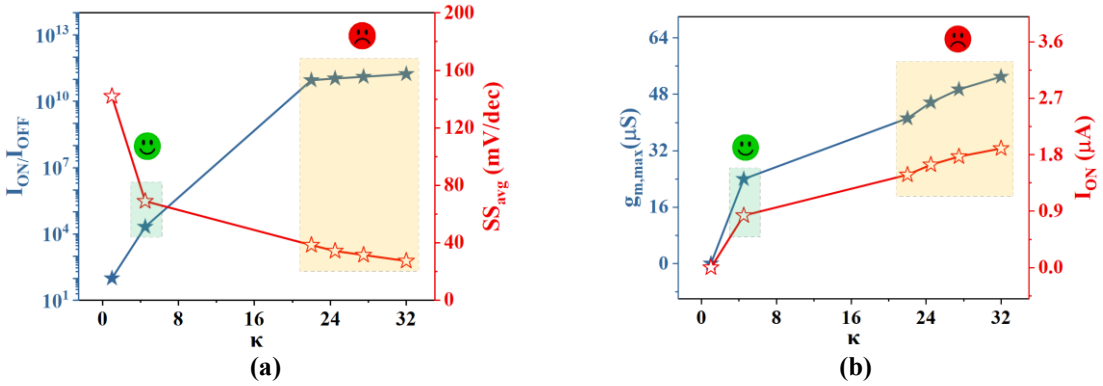


Fig. 4 Variation of the main electrical sensing metrics with effective cavity permittivity: **(a)** I_{ON}/I_{OFF} and SS_{avg} and **(b)** $g_{m,max}$ and I_{ON}, highlighting the separation between the healthy-reference and malignant-associated dielectric conditions.

3.3 Sensitivity Analysis

The relative sensitivity of an electrical parameter A *is defined as [34]*

$$S_A = \left|\frac{A_{bio}-A_{air}}{A_{air}}\right| \quad (5)$$

Because the air-state current is extremely small, air-referenced current sensitivity becomes very large. Therefore, the separation between the healthy and malignant conditions provides a more meaningful measure of disease discrimination. Relative to the healthy condition, I_{ON} increases by approximately 78-129%, while $g_{m,max}$ increases by 71-121% across κ=22-32. In parallel, SS_{avg} decreases by approximately 44-60%. The strongest separation is observed in I_{ON}/I_{OFF}, which increases from 2.12×10^{5} for the healthy condition to 9.11×10^{10}-1.73×10^{11} for the malignant conditions, corresponding to an enhancement of approximately to 4.3×10^{5} to to 8.2×10^{5} relative to the healthy reference. This large electrical contrast provides a clear basis for distinguishing the healthy-reference and malignant-associated dielectric states.

4. Conclusion

A nanocavity-modulated $In_{0.75}Ga_{0.25}N$ gate-engineered dopingless TFET has been investigated as a low-power platform for breast-cancer-associated dielectric sensing. By combining charge-plasma source/drain formation with the retained tunneling gate and a nanocavity beneath the control gate, the proposed structure converts changes in the effective cavity permittivity into pronounced modulation of the energy bands, BTBT probability, and carrier concentration. The air-filled cavity provides an ultra-low-current ready-to-use state, whereas the healthy and malignant-associated dielectric conditions produce clearly distinguishable electrical responses. At V_{GS}=1V and V_{DS}=0.5 V, the I_{ON}/I_{OFF} ratio increases from 2.12×10^{5} for the healthy-reference condition to as high as 1.73×10^{11} for the malignant-associated conditions. Simultaneously, SS_{avg} improves to 27.4 mV/dec, $g_{m,max}$ reaches 53 μS, and I_{ON} reaches 1.9 μA. Despite this enhanced sensing response, the corresponding ON-state power remains below approximately 1 μW. These results demonstrate that the proposed InGaN TFET can provide strong electrical discrimination, steep switching, and ultra-low-power operation, making it a promising device-level platform for future label-free dielectric biosensing applications.

REFERENCES

[1] *Kolay, A., Kumar, A. (2024). A novel liver cancer POC diagnostic detection technique by a gate-engineered source-extended TFET device. Medical Engineering & Physics, vol. 125, article 104133. doi: 10.1016/j.medengphy.2024.104133.*
[2] *Arnold, M., Morgan, E., Rumgay, H., et al. (2022). Current and future burden of breast cancer: Global statistics for 2020 and 2040. The Breast, vol. 66, p. 15–23. doi: 10.1016/j.breast.2022.08.010.*
[3] *Skaane, P., Hofvind, S., Skjennald, A. (2007). Randomized trial of screen-film versus full-field digital mammography with soft-copy reading in population-based screening program: Follow-up and final results of Oslo II study. Radiology, vol. 244, no. 3, p. 708–717. doi: 10.1148/radiol.2443061478.*
[4] *Gupta, R., Beg, S., Singh, S. (2024). Evaluation of design and performance of biosensor utilizing ferroelectric vertical tunnel field-effect transistor (V-TFET). Silicon, vol. 16, p. 3839–3850. doi: 10.1007/s12633-024-02966-1.*
[5] *Al-Foheidi, M., Al-Mansour, M.M., Ibrahim, E.M. (2013). Breast cancer screening: Review of benefits and harms, and recommendations for developing and low-income countries. Medical Oncology, vol. 30, article 471. doi: 10.1007/s12032-013-0471-5.*
[6] *Pal, U., Saxena, M., Vishnu, G.K.A., et al. (2020). Optical spectroscopy-based imaging techniques for the diagnosis of breast cancer: A novel approach. Applied Spectroscopy Reviews, vol. 55, no. 8, p. 778–804. doi: 10.1080/05704928.2020.1749651.*
[7] *Shaveisi, M., Vadizadeh, M., Fallahnejad, M. (2024). Enhanced biosensing with double gate junctionless FET based on III–V compound semiconductor and symmetric cavity for label-free detection of neutral and charged biomolecules. Sensing and Imaging, vol. 25, article 62. doi: 10.1007/s11220-024-00516-y.*
[8] *Dewan, B., Chaudhary, S., Singh, D. (2025). DC and RF/analog performances of dielectric-modulated split-source double gate TFET biosensor: A simulation study. Materials Science and Engineering: B, vol. 313, article 117910. doi: 10.1016/j.mseb.2024.117910.*
[9] *Hussein, M., Awwad, F., Jithin, D., El Hasasna, H., Athamneh, K., Iratni, R. (2019). Breast cancer cells exhibits specific dielectric signature in vitro using the open-ended coaxial probe technique from 200 MHz to 13.6 GHz. Scientific Reports, vol. 9, article 4681. doi: 10.1038/s41598-019-41124-1.*
[10] *Bitra, J., Komanapalli, G. (2023). A dielectric modulated step-channel junction-less TFET (DM-SC-JLTFET) for label-free detection of breast cancer cells: Design and sensitivity analysis. Sensing and Imaging, vol. 24, article 28. doi: 10.1007/s11220-023-00439-0.*
[11] *Vanlalawmpuia, K., Ghosh, P. (2023). Performance assessment of dielectrically modulated negative capacitance germanium source vertical tunnel FET biosensor for detection of breast cancer cell lines. AEÜ – International Journal of Electronics and Communications, vol. 171, article 154902. doi: 10.1016/j.aeue.2023.154902.*
[12] *Choudhary, V., Kumar, M., Chugh, N., Madan, J. (2025). B-VDL-TFET: An ultrascaled, high-sensitivity sensor for breast cancer detection. IEEE Sensors Journal, vol. 25, p. 29820–29829. doi: 10.1109/JSEN.2025.3581081.*
[13] *Gupta, S., Pratap, Y., Gupta, M. (2025). Breast cancer detection using dual nanocavities GaN junctionless FinFET biosensor. Sensing and Imaging, vol. 26, article 15. doi: 10.1007/s11220-025-00544-2.*
[14] *Khodabakhsh, A., Amini, A., Fallahnejad, M. (2024). A multi-directional GaN/TiO2_2 cuboidal nanowire junctionless FET-based ultra-high pressure sensor: A design perspective. Advanced Theory and Simulations, vol. 7, no. 11, article 2400194. doi: 10.1002/adts.202400194.*
[15] *Khodabakhsh, A., Fallahnejad, M., Vadizadeh, M. (2024). A breakthrough for temperature and linearity stability from device to circuit-level with 14 nm junctionless SOI FinFET: Advancing K-band LNA performance. Microelectronics Reliability, vol. 152, article 115278. doi: 10.1016/j.microrel.2023.115278.*
[16] *Khodabakhsh, A., Amini, A., Afzal, A. (2025). Phosphorus-based heterojunction tunnel field-effect transistors: From atomic insights to circuit renovations. Physical Chemistry Chemical Physics, vol. 27, p. 1459–1472. doi: 10.1039/D4CP04121F.*
[17] *Duan, X., Zhang, J., Wang, S., Li, Y., Xu, S., Hao, Y. (2018). A high-performance gate engineered InGaN dopingless tunnel FET. IEEE Transactions on Electron Devices, vol. 65, no. 3, p. 1223–1229. doi: 10.1109/TED.2018.2796848.*
[18] *Kumar, M.J., Janardhanan, S. (2013). Doping-less tunnel field effect transistor: Design and investigation. IEEE Transactions on Electron Devices, vol. 60, no. 10, p. 3285–3290. doi:*

10.1109/TED.2013.2276888.
[19] *Hueting, R.J.E., Rajasekharan, B., Salm, C., Schmitz, J. (2008). The charge plasma P-N diode. IEEE Electron Device Letters, vol. 29, no. 12, p. 1367–1369. doi: 10.1109/LED.2008.2006864.*
[20] *Li, W., Sharmin, S., Ilatikhameneh, H., et al. (2015). Polarization-engineered III-nitride heterojunction tunnel field-effect transistors. IEEE Journal on Exploratory Solid-State Computational Devices and Circuits, vol. 1, p. 28–34. doi: 10.1109/JXCDC.2015.2426433.*
[21] *Li, W., Cao, L., Lund, C., Keller, S., Fay, P. (2016). Performance projection of III-nitride heterojunction nanowire tunneling field-effect transistors. physica status solidi (a), vol. 213, no. 4, p. 905–908. doi: 10.1002/pssa.201532564.*
[22] *Boucart, K., Ionescu, A.M. (2007). Double-gate tunnel FET with high-κ\kappa gate dielectric. IEEE Transactions on Electron Devices, vol. 54, no. 7, p. 1725–1733. doi: 10.1109/TED.2007.899389.*
[23] *Fabien, C.A.M., Gunning, B.P., Doolittle, W.A., Fischer, A.M., Wei, Y.O., Xie, H., Ponce, F. (2015). Low-temperature growth of InGaN films over the entire composition range by MBE. Journal of Crystal Growth, vol. 425, p. 115–118. doi: 10.1016/j.jcrysgro.2015.02.014.*
[24] *Aseev, P., Soto Rodriguez, P.E.D., Gómez, V.J., et al. (2015). Near-infrared emitting In-rich InGaN layers grown directly on Si: Towards the whole composition range. Applied Physics Letters, vol. 106, article 072102. doi: 10.1063/1.4909515.*
[25] *Ochi, R., Maeda, E., Nabatame, T., Shiozaki, K., Sato, T., Hashizume, T. (2020). Gate controllability of HfSiOx_x/AlGaN/GaN MOS high-electron-mobility transistor. AIP Advances, vol. 10, no. 6, article 065215. doi: 10.1063/5.0012687.*
[26] *Kirkpatrick, C., Lee, B., Suri, R., Yang, X., Misra, V. (2012). Atomic layer deposition of SiO2_2 for AlGaN/GaN MOS-HFETs. IEEE Electron Device Letters, vol. 33, no. 9, p. 1240–1242. doi: 10.1109/LED.2012.2203782.*
[27] *Frasconi, M., Mazzei, F., Ferri, T. (2010). Protein immobilization at gold–thiol surfaces and potential for biosensing. Analytical and Bioanalytical Chemistry, vol. 398, no. 4, p. 1545–1564. doi: 10.1007/s00216-010-3708-6.*
[28] *Suni, I.I. (2021). Substrate materials for biomolecular immobilization within electrochemical biosensors. Biosensors, vol. 11, no. 7, article 239. doi: 10.3390/bios11070239.*
[29] *Anand, S., Singh, A., Amin, S.I., Thool, A.S. (2019). Design and performance analysis of dielectrically modulated doping-less tunnel FET-based label-free biosensor. IEEE Sensors Journal, vol. 19, no. 12, p. 4369–4374. doi: 10.1109/JSEN.2019.2900092.*
[30] *Cherik, I.C., Mohammadi, S. (2022). Dielectric modulated doping-less tunnel field-effect transistor, a novel biosensor based on cladding layer concept. IEEE Sensors Journal, vol. 22, no. 11, p. 10308–10314. doi: 10.1109/JSEN.2022.3163475.*
[31] *Silvaco, Inc. (2017). TCAD simulations of TFET and tunneling diode. Simulation Standard, July 2017.*
[32] *Singh, D., Pandey, S., Nigam, K., Sharma, D., Yadav, D.S., Kondekar, P. (2017). A charge-plasma-based dielectric-modulated junctionless TFET for biosensor label-free detection. IEEE Transactions on Electron Devices, vol. 64, no. 1, p. 271–278. doi: 10.1109/TED.2016.2622403.*
[33] *Narang, R., Sasidhar Reddy, K.V., Saxena, M., Gupta, R.S., Gupta, M. (2012). A dielectric-modulated tunnel-FET-based biosensor for label-free detection: Analytical modeling study and sensitivity analysis. IEEE Transactions on Electron Devices, vol. 59, no. 10, p. 2809–2817. doi: 10.1109/TED.2012.2208115.*
[34] *Agrwal, P., Kumar, A. (2025). In0.53_{0.53}Ga0.47_{0.47}As-SOI-FinFET biosensor for ultra-sensitive point-of-care protein biomarker detection. Discover Applied Sciences, vol. 7, article 1435. doi: 10.1007/s42452-025-07953-8.*